Wind and Structures, Vol. 3, No. 4 (2000) 279-289
DOI: http://dx.doi.org/10.12989/was.2000.3.4.279

Wind load combinations and extreme pressure distributions on low-rise buildings

Yukio Tamura†

Department of Architectural Engineering, TIP, 1583 Iiyama, Astugi, Japan

Hirotoshi Kikuchi‡ and Kazuki Hibi‡†

RIT, Shimizu Corporation, Etchujima 3-4-17, Koto-ku, Tokyo, Japan

Abstract. The main purpose of this paper is to demonstrate the necessity of considering wind load combinations even for low-rise buildings. It first discusses the overall quasi-static wind load effects and their combinations to be considered in structural design of low-rise buildings. It was found that the maximum torsional moment closely correlates with the maximum along-wind base shear. It was also found that the instantaneous pressure distribution causing the maximum along-wind base shear was quite similar to that causing the maximum torsional moment, and that this asymmetric pressure pattern simultaneously accompanies considerable across-wind and torsional components. Secondly, the actual wind pressure distributions causing maximum quasi-static internal forces in the structural frames are conditionally sampled and their typical pressure patterns are presented.

Key words : wind load combination; low-rise buildings; quasi-static wind load; pressure distrubution; along-wind base shear; across-wind base shear; torsional moment.

1. Introduction

The necessity of capturing the maximum load effects was first introduced by Davenport (1961) as a gust factor. Solari (1989) attempted to develop Davenport's gust factor technique to more generic maximum load effects based upon the response spectrum technique. Regarding low-rise buildings, Holmes (1988) studied the distributions of instantaneous wind pressures along a gabled roof frame producing the peak loads and load effects on the frame of a low-rise building model. Considerable variation was found in these instantaneous pressure distributions. Tamura *et al*. (1992) discussed the maximum load effects on beams supporting flat roofs based on instantaneous wind pressures simultaneously measured at up to 512 points. The gust response factors for various load effects on rigid and elastic beams were examined and the influence of the turbulence intensity and the integral scale were demonstrated. The load-response-correlation (LRC) method was proposed by Kasperski (1992) to take into account a realistic spatial distribution of wind loads that produce accurate peak structural responses. Holmes (1992) extended Kasperski's LRC approach to incorporate proper

† Professor
‡ Senior Researcher
‡† Researcher

orthogonal decomposition (POD).

The maximum normal stresses in columns are almost proportional to the scalar sum of the bending moments along the two principle axes of the column section, which are caused by the two overall lateral forces and torsional moment acting on a low-rise building. According to the preliminary study, the contributions of the uplift and two overturning moments are not significant. The aim of this paper is to describe the necessity of considering the combined effects of the two lateral wind force components and torsional moment even for low-rise buildings. This is achieved by demonstrating that the instantaneous pressure distribution causing the maximum along-wind base shear is asymmetric and quite similar to that causing the maximum torsional moment, thus simultaneously producing considerable effects of across-wind and torsional components. In addition to these wall pressure effects, the roof pressure effects are examined by checking the instantaneous pressure distributions causing the maximum internal forces on the roof beams of frames normal and parallel to the wind.

2. Wind tunnel data

Fluctuating wind pressure records obtained in a boundary layer wind tunnel 2.6 m wide $\times$ 2.4 m high were analyzed. Two building models with flat roofs were tested in a turbulent shear flow as shown in Table 1, where B and D are the dimensions of the building plan and H is the height. The wind direction was normal to the wall of length B. The geometrical scale of the turbulent shear flow was 1/250, and the power law index α of the mean wind speed profile was set at $\alpha = 1/4$. Wind pressures at 416 and 512 locations uniformly distributed on the surfaces of Type 1 Model and Type 2 Model, respectively, were simultaneously sampled every 0.00128s. The total sample length was 62.91s (49152 data) for Type 1 Model and 41.94s (32768 data) for Type 2 Model. Tubing effects were numerically compensated by the gain and phase shift characteristics of the pressure measurement system using the method reported in Ueda, Hibi, Tamura and Fujii (1994).

3. Wind load combinations acting on low-rise building models

3.1. Quasi-static along-wind base shear, across-wind base shear and torsional base moment

The fluctuating pressures were integrated to obtain the quasi-static base shear F_D and F_L and the base moment M_T. They are expressed in non-dimensional forms based on the mean velocity pressure q_H at roof height: along-wind shear force coefficient $C_D = F_D / q_H BH$, across-wind shear force coefficient $C_L = F_L / q_H BH$, and the torsional moment coefficient $C_T = M_T / q_H BHR$, where $R = (B^2 + D^2)^{1/2} / 2$

Table 1 Model dimensions

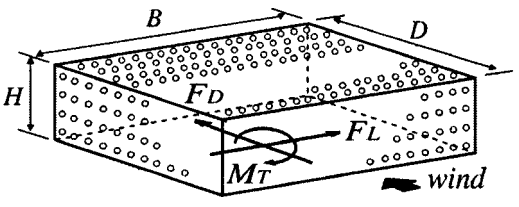

Model	B (mm)	D (mm)	H (mm)
Type 1	170	120	50
Type 2	200	200	50

3.2. Combinations of quasi-static load effects at the base

The wind tunnel records were divided into sub-runs whose lengths corresponded to almost 10 min in full-scale, and eighteen 10 min runs were obtained for each model. From each 10 min run, the maximum value of one of the load effects, i.e., along-wind base shear, across-wind base shear or torsional base moment, was selected and the other two load effects simultaneously recorded were picked up. For example, across-wind base shear coefficient and torsional base moment coefficient are picked up at the moment when the maximum along-wind base shear coefficient C_{Dmax} was recorded, and they are indicated as $C_L(C_{Dmax})$ and $C_T(C_{Dmax})$. The other combinations $\{C_{Lmax}, C_D(C_{Lmax})$ and $C_T(C_{Lmax})\}$ and $\{C_{Tmax}, C_D(M_{Tmax})$ and $C_L(M_{Tmax})\}$ were also captured when the maximum across-wind base shear and the maximum torsional base moment, respectively, were recorded.

3.3. Load effect combinations

Figs. 1(a)-(f) show the results for Type 1 Model when the maximum along-wind base shear coefficient C_{Dmax} was recorded. Fig. 1(a) shows the combination of maximum along-wind base shear coefficient C_{Dmax} and the simultaneously recorded across-wind base shear coefficient $C_L(C_{Dmax})$. The mean value and coefficient of variation (COV) of C_{Dmax} are 2.6 and 19%, respectively. Here, the turbulence intensity of the wind speed at the roof height was 29%. $C_L(C_{Dmax})$ lies between 0.1 and 0.7. The ordinate of Fig. 1(b) shows the across-wind base shear ratio $C_L(C_{Dmax}) / C_{Lmax}$, which is the ratio of the simultaneously recorded across-wind base shear coefficient $C_L(C_{Dmax})$ to its maximum value C_{Lmax} for each 10min run. When the maximum along-wind base shear C_{Dmax} occurs, 10% - 70% of the maximum across-wind base shear was simultaneously recorded. Fig. 1(c) shows the relative

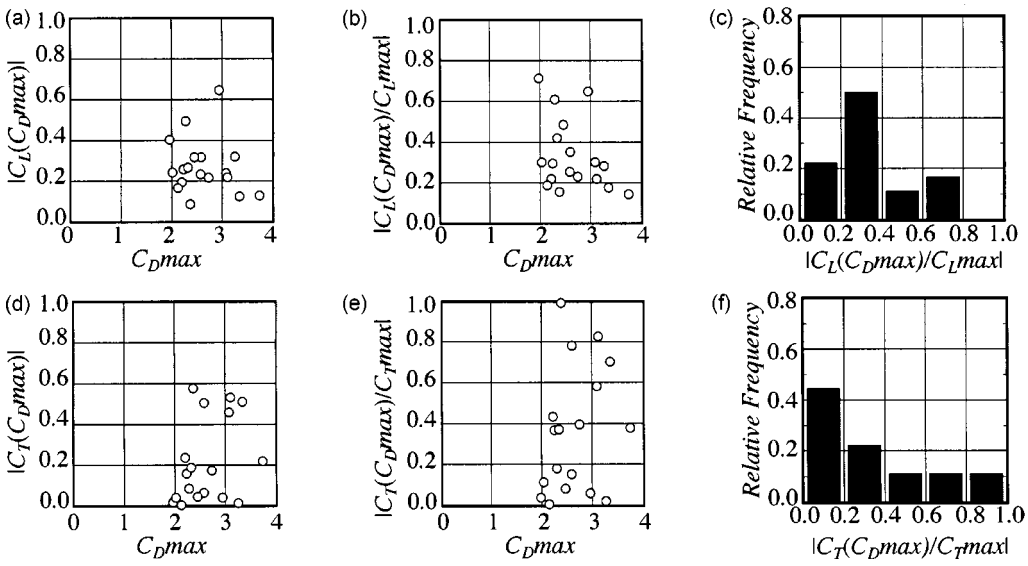

Fig. 1 Across-wind base shear and torsional base moment accompanied by maximum along-wind base shear C_{Dmax} (Type 1 Model), (a) Across-wind base shear coefficient $C_L(C_{Dmax})$, (b) Across-wind base shear ratio $C_L(C_{Dmax}) / C_{Lmax}$, (c) Relative frequency of $C_L(C_{Dmax}) / C_{Lmax}$, (d) Torsional base moment coefficient $C_T(C_{Dmax})$, (e) Torsional base moment ratio $C_T(C_{Dmax}) / C_{Tmax}$, (f) Relative frequency of $C_T(C_{Dmax}) / C_{Tmax}$

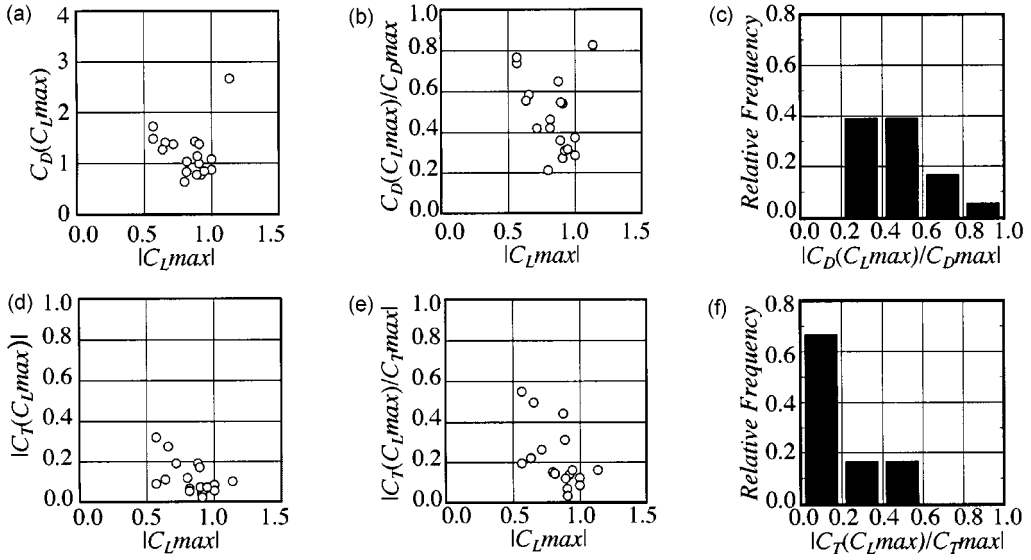

Fig. 2 Along-wind base shear and torsional base moment accompanied by maximum across-wind base shear C_{Lmax} (Type 1 Model), (a) Along-wind base shear coefficient $C_D(C_{Lmax})$, (b) Along-wind base shear ratio $C_D(C_{Lmax})/C_{Dmax}$, (c) Relative frequency of $C_D(C_{Lmax})/C_{Dmax}$, (d) Torsional base moment coefficient $C_T(C_{Lmax})$, (e) Torsional base moment ratio $C_T(C_{Lmax})/C_{Tmax}$, (f) Relative frequency of $C_T(C_{Lmax})/C_{Tmax}$

frequency of the across-wind base shear ratio $C_L(C_{Dmax})/C_{Lmax}$. Figs. 1(d)-(f) are for the torsional base moment coefficient $C_T(C_{Dmax})$ accompanied by the maximum along-wind base shear. The value of $C_T(C_{Dmax})$ lies between 0 and 0.6, and between 0% and 100% of the maximum torsional moments were simultaneously recorded with the maximum along-wind base shear.

Figs. 2(a) - (f) show the cases where the maximum across-wind base shear coefficient C_{Lmax} was recorded. The mean value and COV of C_{Lmax} are 0.84 and 18%, respectively. When the maximum across-wind base shear C_{Lmax} occurs, 20% - 80% of the maximum along-wind base shear were simultaneously recorded. 30% - 60% of the maximum along-wind base shear appeared most frequently. The value of $C_T(C_{Lmax})$ lies between 0 and 0.4, and between 0% and 60% of the maximum torsional moments were simultaneously recorded with the maximum across-wind base shear.

Figs. 3(a) - (f) show quite interesting results when the maximum torsional base moment C_{Tmax} was recorded. It should be noted that Fig. 3(a) shows clear correlation between the maximum torsional base moment coefficient C_{Tmax} and the simultaneously recorded along-wind base shear coefficient $C_D(C_{Tmax})$. The mean value and COV of $C_D(C_{Tmax})$ are 0.56 and 20%, respectively. When the maximum torsional base moment C_{Tmax} occurs, 60% - 100% of the maximum along-wind base shear was simultaneously recorded. As shown in Fig. 3(c), 70% - 90% of the maximum along-wind base shear appears most frequently. The value of $C_L(C_{Tmax})$ lies between 0 and 0.4, and between 0% and 40% of the maximum across-wind base shear were simultaneously recorded with the maximum torsional base moment. These figures clearly demonstrate that almost the largest level of along-wind base shear jointly happens with the maximum torsional base moment. This suggests that the flow patterns causing the maximum along-wind base shear and the maximum torsional base moment might be almost the same, while the flow pattern causing the maximum across-wind base shear might be different.

Almost the same results were obtained for Type 2 Model.

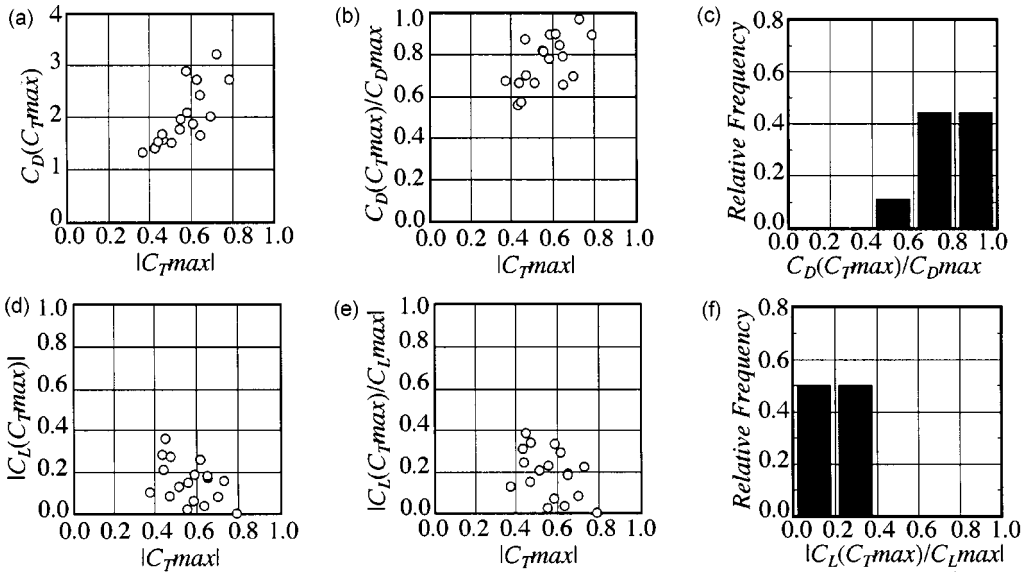

Fig. 3 Along-wind base shear and across-wind base shear accompanied by maximum torsional base moment C_{Tmax} (Type 1 Model), (a) Along-wind base shear coefficient $C_D(C_{Tmax})$, (b) Along-wind base shear ratio $C_D(C_{Tmax}) / C_{Dmax}$, (c) Relative frequency of $C_D(C_{Tmax}) / C_{Dmax}$, (d) Across-wind base shear coefficient $C_L(C_{Tmax})$, (e) Across-wind base shear ratio $C_L(C_{Tmax}) / C_{Lmax}$, (f) Relative frequency of $C_L(C_{Tmax}) / C_{Lmax}$

3.4. Cross-correlation coefficients between wind load effects at the base

Figs. 4(a) - (c) show examples of cross-correlation coefficients between the three components of wind load effects at the base for Type 1 Model. Here, the time lag τ is converted to the full-scale time lag in the figures. Almost no correlation is seen between along-wind shear and across-wind shear, or between along-wind shear and torsional moment. The former coincides with the aforementioned results, demonstrating a low correlation between the maximum along-wind shears and across-wind shears. However, the latter does not, thus suggesting a high correlation between the maximum torsional moment and along-wind shear seen in Fig. 3(b).The across-wind shear and torsional moment have

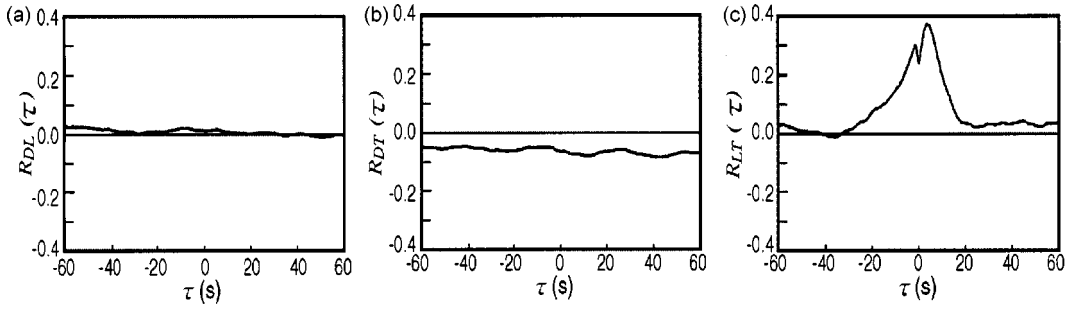

Fig. 4 Cross-correlation coefficients between load effects at base (Type 1 Model): (a) Along-wind and across-wind base shears; (b) Along-wind base shear and torsional base moment; (c) Across-wind base shear and torsional base moment

some correlation, as shown in Fig. 4(c), although their maximum values do not correlate, as seen in Fig. 3(e).

These contradictory relations between the temporal average correlation of the time series and the correlation of the maximum values suggest that the extreme events can be different from the temporal average characteristics. It at least suggests that the normal cross-correlation has a limitation in examining the combination of the extreme events.

Type 2 Model provided almost the same results.

4. Instantaneous wind pressure distributions causing maximum quasi-static load effects

4.1. Quasi-static base shear and torsional base moment

To examine the exact wind pressure pattern causing the quasi-static load effects, twelve runs corresponding to almost 10min in full-scale were obtained for Type 2 Model.

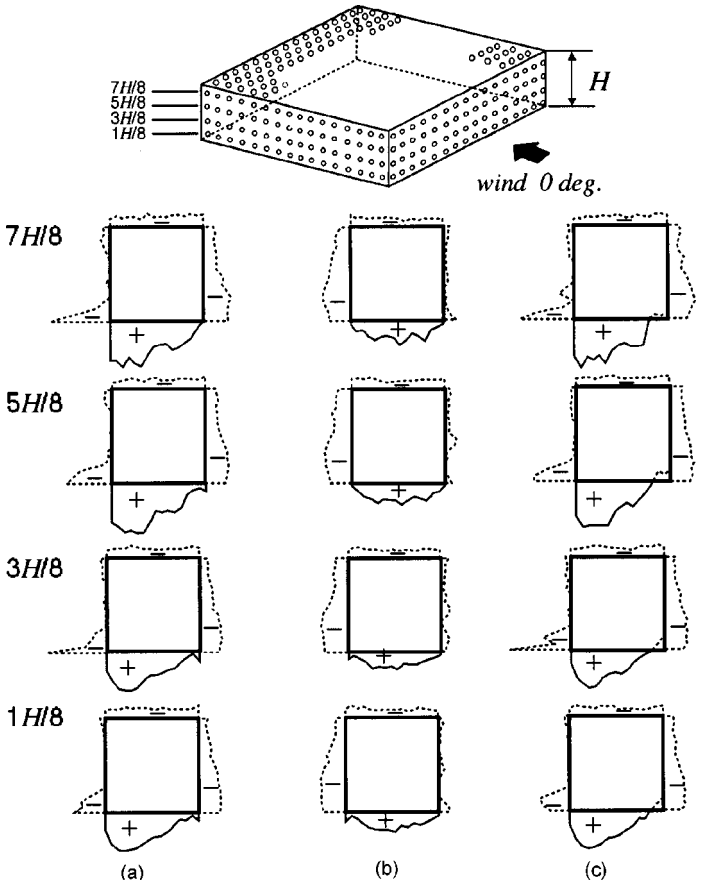

Fig. 5 Examples of instantaneous wind pressure distributions causing maximum load effects (a) Causing maximum along-wind base shear, (b) Causing maximum across-wind base shear, (c) Causing maximum torsional base moment

Figs. 5(a), (b) and (c) show examples of the instantaneous wind pressure distributions at four layers: (7/8)*H*, (5/8)*H*, (3/8)*H* and (1/8)*H*, when the maximum along-wind base shear, the maximum across-wind base shear, and the maximum torsional base moment, respectively, were recorded. The different wind pressure patterns appear for the different maximum load effects, but there is no significant difference between the pressure patterns on the four layers.

Figs. 6(a), (b) and 6(c) show the instantaneous wind pressure distributions when the maximum load effects were recorded for the twelve 10min runs. Here, the pressure distributions are only for the top layer (7/8)*H*, and the first pressure pattern for each load effect corresponds to Fig. 5.

Fig. 6(a) shows the instantaneous wind pressure distributions when the maximum along-wind base shear was recorded, and a typical pressure pattern is recognized among the twelve samples. The circle arrow in the figure indicates the direction of the torsional base moment as a measure of the asymmetric pressure pattern. The positive pressure on the windward wall is high and clusters on the left side or the right side, depending on the sample. A local high suction tends to appear near the leading edge of the left side wall or the right side wall, depending on the sample. This asymmetric

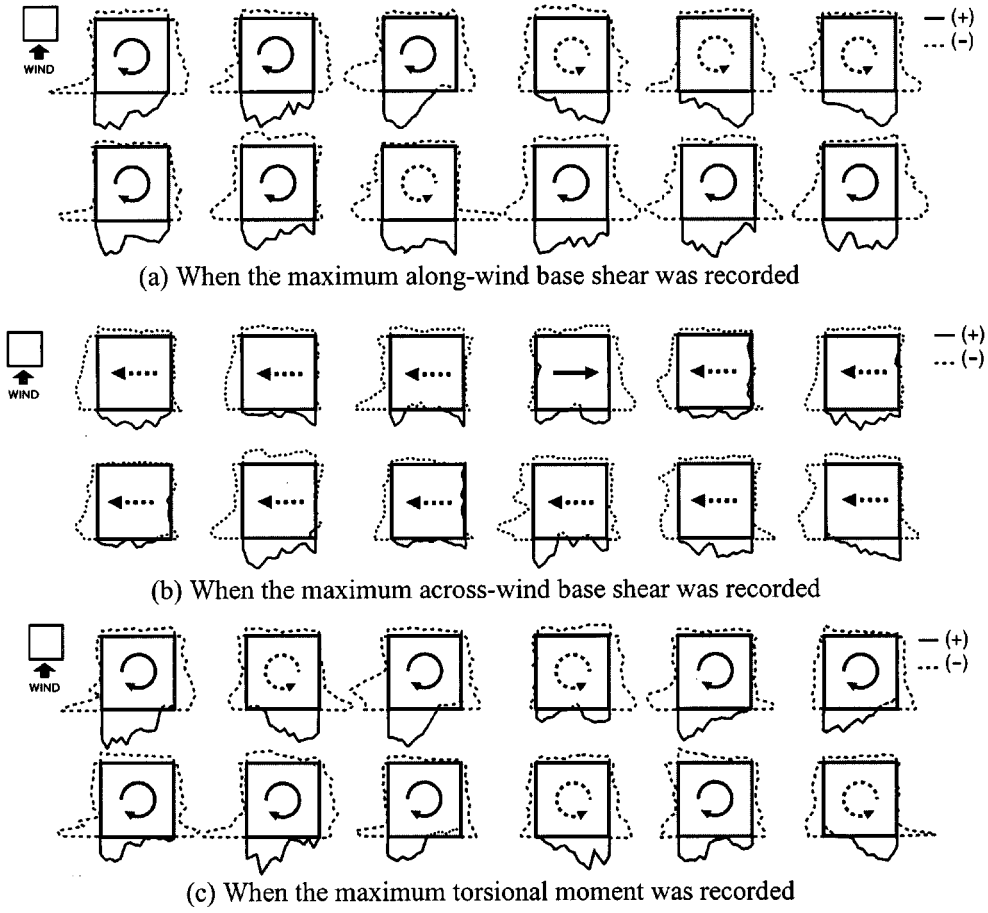

Fig. 6 Instantaneous wind pressure distributions causing maximum load effects at the base (Type 2 Model, (7/8)*H*)

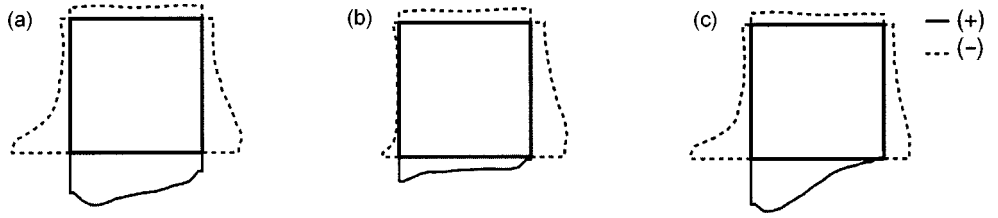

Fig. 7 Ensemble-average instantaneous pressure distributions causing maximum load effects (Type 2 Model, (7/8)H), (a) Maximum along-wind base shear, (b) Maximum across-wind base shear, (c) Maximum torsional base moment

pressure pattern is the special feature of the instantaneous pressure distribution causing the maximum along-wind base shear. As the torsional base moments of some samples are clockwise and those of others are anti-clockwise, it is obvious that the asymmetric pressure patterns are not due to the inclination of the wind tunnel flow nor to any model irregularity. This implies that the maximum drag is generated at an instance when the wind direction is slightly inclined to one side.

Fig. 6(b) shows the twelve samples of the instantaneous wind pressure distribution when the maximum across-wind base shear was recorded. The negative pressure on one side wall is large, while that on the other is nearly zero. Here, the arrow indicates the direction of the across-wind base shear.

Fig. 6(c) shows the twelve samples of the instantaneous wind pressure distribution when the maximum torsional base moment was recorded. As was already seen in Fig. 5, the pressure distributions for the maximum torsional base moments are similar to the cases for the maximum along-wind base shear shown in Fig. 6(a). This result coincides with the fact that the largest level of the along-wind base shear is accompanied by the maximum torsional moment, as seen in Fig. 3(a).

For ease of comparison, the ensemble-average pressure patterns causing the maximum load effects are discussed. If the pressure patterns shown in Fig. 6(a) are superimposed and averaged, a pressure pattern similar to the mean pressure distribution may be obtained, rather than the typical pressure pattern causing the maximum along-wind base shear. Therefore, the right and left of some figures are turned to match the asymmetric pressure patterns in the same direction considering the circle arrows in Figs. 6(a) and 6(c) and the straight arrows in Fig. 6(b). Then, the ensemble-average pressure patterns were obtained for the three load effects at the base as shown in Figs. 7(a)-(c).

4.2. Bending moment and shear force in structural frames

The quasi-static bending moment and shear force were analyzed at various design points in Frames A and B for Type 2 Model. The plane of Frame A is parallel to the wind direction and that of Frame B is normal to wind. Three different supporting conditions at the column bases, i.e., pin - roller, pin - pin and fixed - fixed, were examined. Frames A and B are set at the center row and the end row of the pressure tap arrangement, and the fluctuating wind loads acting on the frames were directly applied at the pressure tap positions based on the wind tunnel pressure data. Fig. 8 shows examples of instantaneous pressure distributions causing maximum quasi-static load effects.

Figs. 8(a) and 8(b) show the cases of maximum bending moment and shear force, respectively, at the windward end of the roof beam of Frame A with pin-roller base conditions. High suction near the windward roof edge and large positive pressures on the windward wall are typical features of

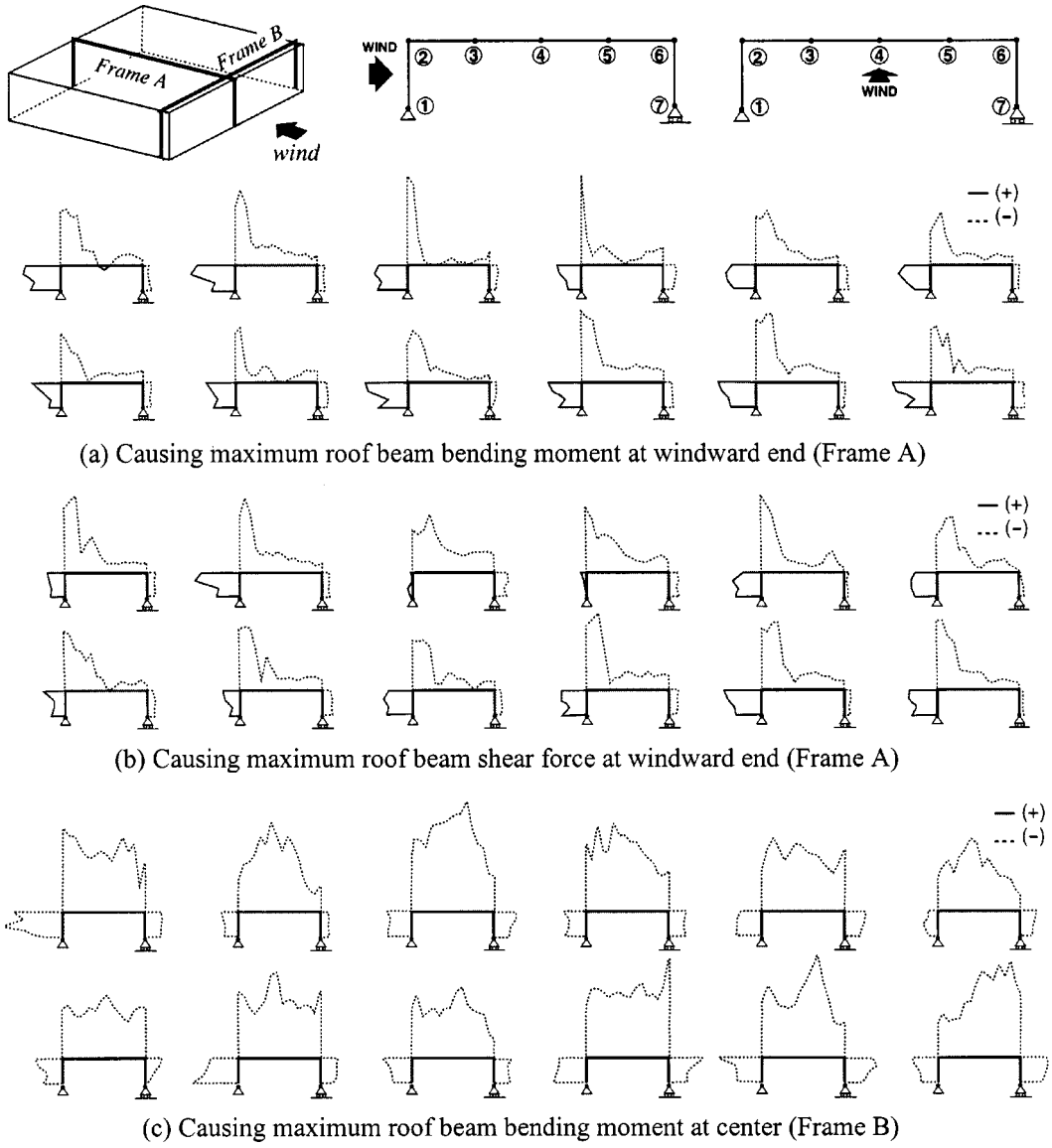

Fig. 8 Instantaneous pressure distributions causing maximum quasi-static load effects at some design points in pin-roller frames for Type 2 Model

both pressure patterns. Fig. 8(c) shows the case of bending moment at the beam center of Frame B with pin-roller condition. As Frame B is located near the windward end, high suction due to flow separation covers its whole span and the frame at this location occasionally becomes critical in design. The high suction covers almost the whole span and a gentle peak near the roof center is also seen in the pressure patterns of Fig. 8(c).

The extreme pressure patterns vary with the design points, the load effects and column base conditions, and they are not necessarily the same as the mean pressure distribution, as Holmes (1988) pointed out.

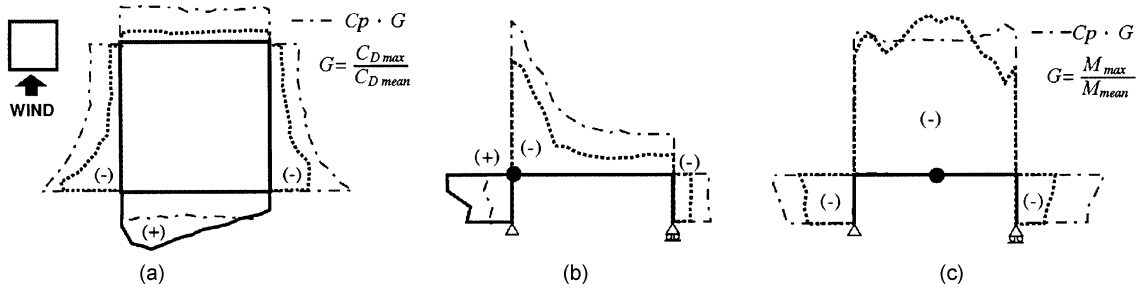

Fig. 9 Ensemble-average instantaneous pressure distributions causing maximum load effects (Type 2 Model): (a) Maximum along-wind base shear; (b) Maximum roof beam bending moment at windward end (Frame A, Pin-roller); (c) Maximum roof beam bending moment at center (Frame B, Pin-roller)

4.3. Comparisons of wind pressure distribution causing maximum load effects with mean pressure distributions

Figs. 9(a)-(c) show examples of comparisons of ensemble-average pressure patterns (solid line: +, dotted line –) causing maximum load effects and the mean pressure distributions (broken line with dot). The mean pressure distributions C_p are multiplied by the ensemble-average gust loading factor G for each load effect.

The pressure patterns vary especially on the windward wall, depending on the column base support conditions. They also vary depending upon the flow conditions. It is obvious that the mean pressure distributions are not necessarily appropriate for design wind loads as already pointed out by Holmes (1988) and Kasperski (1992).

5. Conclusions

Various load effect combinations have been examined on the basis of multi-channel wind tunnel pressure data, and the actual wind pressure distributions causing the maximum quasi-static load effects are conditionally sampled and examined.

The instantaneous pressure distribution causing the maximum along-wind base shear is found to be asymmetric and quite similar to that causing the maximum torsional moment, thus simultaneously producing considerable effects of across-wind and torsional components. This suggests the necessity to consider the combined effects of the two lateral wind force components and torsional moment even for low-rise buildings. The close correlation of maximum torsional moment and maximum along wind base shear is clearly seen, although their temporal average characteristics represented by cross-correlation show only slight correlation. Further investigation should be interesting on this point, but it suggests the possibility that extreme events show somewhat different behaviour from the normal temporal average tendency. In examining the above new findings, concerns about distortion of wind tunnel flow, model shape accuracy, and high frequency error in fluctuating pressure signals were carefully checked, but no serious problem was found. Satisfactory symmetric mean pressure distributions shown in Fig. 9 support this.

The roof pressure effects were also examined by checking the instantaneous pressure distributions causing the maximum internal forces on the roof beams of frames normal and parallel to the wind. The typical pressure patterns causing several load effects were obtained, verifying the limitation of

applying the mean pressure distribution as the design wind load as pointed out by Holmes and Kasperski.

References

Davenport, A. G. (1961), "The application of statistical concepts to the wind loading of structures", *Proceedings, Institution of Civil Engineers*, London, **19**, 449-472.

Holmes, J. D. (1988), "Distribution of peak wind loads on a low-rise building", *Journal of Wind Engineering and Industrial Aerodynamics*, **29**, 59-67.

Holmes, J. D. (1992), "Optimised peak load distributions", *Journal of Wind Engineering and Industrial Aerodynamics*, **41-44**, 267-276.

Kasperski, M. (1992), "Extreme wind load distributions for linear and nonlinear design", *Engineering Structures, The Journal of Earthquake, Wind and Ocean Engineering*, **14**(1), 27- 34.

Solari, G. (1989), "Wind response spectrum", *Journal of Engineering Mechanics, ASCE*, **115**(6), 2057-2073.

Tamura, Y., Fujii, K. and Ueda, H. (1992), "Design wind loads for beams supporting flat roofs", *Journal of Wind Engineering and Industrial Aerodynamics*, **43**, 1841-1851.

Ueda, H., Hibi, K., Tamura, Y. and Fujii, K. (1994), "Multi-channel simultaneous fluctuating pressure measurement system and its application", *Journal of Wind Engineering and Industrial Aerodynamics*, **51**, 93-104.

(*Communicated by Giovanni Solari*)